Impacts of Carbonate Buffering on Atmospheric Equilibration of CO_2, $\delta^{13}C_{DIC}$, and $\Delta^{14}C_{DIC}$ in Rivers and Streams

Matthew J. Winnick[1], Brian Saccardi[1]

[1] Dept. of Earth, Geographic, and Climate Sciences, University of Massachusetts Amherst
Corresponding Author: Matthew Winnick (mwinnick@umass.edu)

Key Points:

- We develop models of stream CO_2 degassing that include carbonate buffering and apply across a range of alkalinities and stream processes
- Carbonate buffering can support significant contributions to stream CO_2 fluxes but cannot support elevated downstream CO_2 concentrations
- Stable and radio- carbon isotopes are highly impacted by carbonate buffering and can be leveraged to partition carbon sources

Abstract

Rivers and streams play an important role within the global carbon cycle, in part through emissions of CO_2 to the atmosphere. However, the sources of this CO_2 and their spatiotemporal variability are difficult to constrain. Recent work has highlighted the role of carbonate buffering reactions that may serve as a source of CO_2 in high alkalinity systems. In this study, we seek to develop a quantitative framework for the role of carbonate buffering in the fluxes and spatiotemporal patterns of CO_2 and the stable and radio- isotope composition of dissolved inorganic carbon (DIC). We incorporate DIC speciation calculations of carbon isotopologues into a stream network CO_2 model and perform a series of experiments, ranging from the degassing of a groundwater seep to the simulation of 5th-order stream network. We find that carbonate buffering reactions contribute >60% of emissions in high-alkalinity, moderate GW-pCO_2 environments that may characterize carbonate bedrock systems. However, atmosphere equilibration timescales of pCO_2 are minimally affected, which contradicts hypotheses that carbonate buffering maintains high pCO_2 across Strahler orders in high alkalinity systems. In contrast, alkalinity dramatically increases isotope equilibration timescales, which significantly complicates isotopic methods of CO_2 source partitioning by decoupling pCO_2 from isotopic composition even under low alkalinity. Based on similar impacts on atmospheric equilibration for stable and radio- carbon isotopologues, we develop a quantitative method for distinguishing groundwater from stream corridor CO_2 sources in carbonate-dominated watersheds. Together, these results provide a framework to guide fieldwork and interpretations of stream network CO_2 patterns across variable alkalinities.

Plain Language Summary

Streams emit a lot of carbon dioxide (CO_2) to the atmosphere, but it is difficult to figure out where the CO_2 originates. One source is a chemical reaction called carbonate buffering, which happens between different forms of dissolved carbon. This reaction may be important in streams with high alkalinity, but we lack knowledge about how it contributes across different alkalinities and scales. Some studies use isotopes of carbon to trace where CO_2 comes from and how it is released, but we lack knowledge about how carbonate buffering affects isotope patterns. Here, we create mathematical models of CO_2 is production and release including isotopes in streams. Our findings show that carbonate buffering can be a significant source of CO_2 in streams with high alkalinity. However, it doesn't keep CO_2 levels consistently high downstream, as studies previously suggested. Conversely, carbonate buffering has a big effect on patterns of carbon isotopes. This means that common isotope methods for identifying carbon sources streams don't work well. Instead, we propose a way to use stable and radioactive carbon isotopes together to determine the sources of carbon. Our study aims to guide future work and help understand how carbonate buffering impacts CO_2 patterns across stream environments.

1. Introduction

Rivers and streams are increasingly recognized as integral components of the terrestrial carbon cycle (Cole et al., 2007; Drake et al., 2018; Raymond et al., 2013), through which CO_2 produced both in the terrestrial subsurface and within stream corridor environments is released to the atmosphere (e.g. Hotchkiss et al., 2015). Current estimates suggest global CO_2 emissions from

inland waters are roughly half as large as anthropogenic emissions and comparable the net terrestrial carbon sink (DelSontro et al., 2018; Friedlingstein et al., 2022; Gómez-Gener et al., 2021; Lauerwald et al., 2023; Raymond et al., 2013; Sawakuchi et al., 2017); thus, the ability to quantify the magnitude and variability of these fluxes is necessary for gauging terrestrial climate feedbacks. Despite their importance in the terrestrial carbon cycle, the relative balance of CO_2 sources that support carbon fluxes to the atmosphere, which include soil respiration, subsurface chemical weathering reactions, hyporheic zone respiration, and net water-column respiration, remains uncertain. More recently, studies have shown the potential role of carbonate buffering reactions to contribute to evasion fluxes and spatial patterns of stream pCO_2 (Duvert et al., 2019; Kirk & Cohen, 2023; Stets et al., 2017; Wang et al., 2021). Crucially, these buffering dynamics are not typically included in stream carbon budgets and may represent an overlooked aspect of terrestrial-aquatic carbon cycling.

Carbonate buffering reactions are historically well-described within the ocean carbon literature (Broecker et al., 1979; Revelle & Suess, 1957); however, relatively few studies have investigated these dynamics in terrestrial water systems where alkalinity and dissolved CO_2 concentrations vary by orders of magnitude. Briefly, dissolved CO_2 is subject to the reaction,

$$CO_{2(aq)} + H_2O \leftrightarrow H^+ + HCO_3^- \quad \text{(Eq. 1)}.$$

This reaction on its own does not alter alkalinity, and essentially acts to 'store' dissolved CO_2 at levels above what would be predicted using Henry's law alone. Conceptually, the role of this CO_2 'storage' can be demonstrated through the application of Le Chatelier's principle, by which a reaction will occur to partially negate any changes to a system: (1) as dissolved CO_2 concentrations increase, for example as rainfall equilibrates with soil environment pCO_2 during infiltration, this causes Eq. 1 to move from left to right, 'storing' CO_2 in the form of HCO_3^- + H^+; (2) when CO_2 concentrations decrease, for example as groundwater enters streams and equilibrates with the atmosphere, Eq. 1 moves from right to left, acting to replenish dissolved CO_2 concentrations as degassing proceeds. Importantly, the amount of CO_2 that can be 'stored' in this manner increases with increasing alkalinity (Broecker et al., 1979; Revelle & Suess, 1957).

These storage dynamics have been shown to operate within stream systems, and particularly in those with high alkalinity. In a compilation of US stream data, Stets et al. (2017) showed that diurnal changes in dissolved CO_2 reflecting stream metabolism are smaller than diurnal DIC changes, and that this difference increases with higher stream alkalinity. This effect leads to temporal hysteresis in CO_2:O_2 ratios as DIC concentrations take longer to adjust than O_2 to changing metabolic rates. Further, Stets et al. (2017) suggest that this effect may be responsible for observations of high downstream pCO_2 in high alkalinity streams despite significant degassing during downstream transport. These buffering reactions may also contribute significantly to total stream emissions (e.g. Kirk & Cohen, 2023); for example, Duvert et al. (2019) found that up to 60% of emissions were supported by carbonate buffering at some locations within a high alkalinity, tropical Australian river system.

Carbonate buffering dynamics also impact the evolution of carbon isotopes in DIC (e.g. Venkiteswaran et al., 2014), both in terms of stable carbon ratios ($\delta^{13}C$) and radiocarbon ratios ($\Delta^{14}C$); however, these effects have not been explored in detail within stream and river systems. Stable carbon isotopes are frequently used to partition DIC sources, as respired organic carbon,

DIC from carbonate mineral weathering, and atmospheric CO_2 have distinct isotope compositions (e.g. Campeau et al., 2017, 2018; Polsenaere & Abril, 2012). Further, the evolution of $\delta^{13}C$ values along stream reaches may provide information on degassing rates as ^{12}C is preferentially lost to the atmosphere, reflecting both kinetic fractionation of diffusion and equilibration with atmospheric CO_2 which often has a higher $\delta^{13}C_{CO2}$ value than stream waters. Measured $\Delta^{14}C_{DIC}$ values may also be used to partition DIC sources via their age characteristics (Cole et al., 2022; Sveinbjörnsdóttir et al., 2020). For example, respiration of modern organic matter represents near-atmospheric $\Delta^{14}C$ values, while respiration of geogenic organic carbon and weathering of carbonate rock results in low $\Delta^{14}C$ values. The distances over which $\Delta^{14}C$ equilibrates with the atmosphere and how carbonate buffering reactions impact this equilibration have not, to our knowledge, been investigated; however, we hypothesize that these dynamics are crucial in shaping $\Delta^{14}C$ patterns in streams and in determining CO_2 sources.

Here we develop a parsimonious model to investigate how carbonate buffering reactions impact atmospheric equilibration of river and stream DIC pools in terms of overall CO_2 fluxes and equilibration timescales. While this investigation is model-based, the thermodynamic principles that underlie these equations have been long-established. Rather than a direct model-observation comparison, these model experiments are used to develop a generalizable framework to better conceptualize the role of carbonate buffering in terrestrial-aquatic carbon cycling and guide sampling strategies and data interpretation schemes across a broad range of environments.

2. Methods

2.1 Carbonate System Geochemistry

To model the speciation of DIC in terrestrial streams and rivers, we incorporate reactions representing the dissolution of CO_2 gas in water, the dissociation of $CO_{2(aq)}$ (defined here as equivalent carbonic acid, $H_2CO_{3(aq)}$), and the dissociation of bicarbonate as applied separately to ^{12}C, ^{13}C, and ^{14}C DIC species. These reactions and their associated equilibrium constants at 25° C are shown in Table 1, and are based on the methodology of Druhan et al. (2021). Briefly for a given reaction x, the ratio of equilibrium constants (K_x) for DIC isotopologues sets the equilibrium fractionation factor as,

$$\alpha_x = \frac{K_x^i}{K_x^{12}} \qquad \text{(Eq. 2)},$$

where i represents either ^{13}C or ^{14}C versions of reaction x. We use the equilibrium constants of Druhan et al. (2021) for ^{13}C and ^{14}C assuming that fractionation factors are doubled for ^{14}C relative to ^{13}C based on their relative mass differences with ^{12}C.

2.2 Evolution of the carbonate system during degassing

To model the evolution of stream DIC concentrations and isotopic composition during degassing, we simulate three distinct scenarios of increasing complexity:

- Scenario 1: A groundwater seep degassing with no additional CO_2 inputs
- Scenario 2: A groundwater seep degassing with ongoing groundwater inputs and net respiration during downstream transport

- Scenario 3: An 87 km^2 watershed river network in Gothic, CO for which we have previously developed and validated a reactive transport model incorporating groundwater inputs, water-column net respiration and hyporheic zone CO_2 sources.

These scenarios and the processes incorporated into each are diagrammed conceptually in Fig. 1.

2.2.1 Scenario 1: Groundwater degassing with no additional sources

In Scenario 1, we model a groundwater parcel degassing during stream transport with no additional carbon sources during transport (Fig. 1a). This would correspond physically to a spring seep with no additional along-stream groundwater inputs or net respiration. In this scenario, the changes in DIC concentrations are modeled as,

$$\frac{\partial DIC}{\partial t} = -k_{CO2}\left(CO_{2(aq)} - CO_{2(aq)sat}\right) \quad \text{(Eq. 3)},$$

where k_{CO2} is the reaeration coefficient of CO_2, $CO_{2(aq)}$ is the dissolved CO_2 concentration, and $CO_{2(aq)sat}$ is the theoretical concentration of CO_2 in equilibrium with an atmospheric pCO_2 of 410 ppm.

We assume an initial DIC value of groundwater (DIC_{gw}) based on a specified groundwater pCO_2 (20,000 ppm) and alkalinity, which ranges in our experiments from 0 – 6 meq/L based on the range of freshwater stream values from a compilation of United States surface waters (Stets et al., 2017); the resulting DIC_{GW} is calculated as 0.179 – 6.15 mM depending on alkalinity using a temperature of 25° C. We additionally specify a k_{CO2} value (0.05 s^{-1}); however, our analysis examines CO_2 evolution over a non-dimensional timescale (t*) calculated as $t^*=(t)(k_{CO2})$ (unitless); thus, results are scalable to any given k_{CO2} value. The model is then solved using an explicit numerical approximation over discretized timesteps. At each timestep following the calculation of a new DIC value, the carbonate system is speciated using alkalinity and the updated DIC concentration, following the methods of Venkiteswaran et al. (2014). Briefly, we develop a system of equations based on the equilibrium constants in Table 1, along with equations for alkalinity (*Alk*) and DIC as,

$$Alk = [HCO_3^-] + 2[CO_3^{2-}] + [OH^-] - [H^+] \quad \text{(Eq. 4) and}$$

$$DIC = \left[CO_{2(aq)}\right] + [HCO_3^-] + [CO_3^{2-}] \quad \text{(Eq. 5), respectively.}$$

Model calculation scripts using R software are included in the Supplementary Materials.

We solve Eq. 3 and speciate the DIC pool separately for each isotopologue of carbon. For simplicity, we assume that reaeration coefficients are the same for $^{12}CO_2$, $^{13}CO_2$, and $^{14}CO_2$. While molecular diffusion imparts mass-dependent kinetic fractionation (e.g. Zhang et al., 1995), turbulent atmospheric exchange which dominates in most river systems likely does not. We note that our equations are flexible to incorporate kinetic fractionation as,

$$\alpha_k = \frac{k^i}{k^{12}} \quad \text{(Eq. 6)},$$

where *i* denotes the reaeration coefficient *k* for either $^{13}CO_2$ or $^{14}CO_2$, following the formulation of Zhang et al. (1995). We also note that within our model simulations, ^{12}C degasses faster than ^{13}C due to a larger proportional offset between atmospheric and stream $^{12}CO_2$ concentrations. This causes apparent fractionation as the stream equilibrates with atmospheric boundary conditions; however, it does not physically represent kinetic fractionation. We note that these two processes that cause increasing $\delta^{13}C$ values during degassing are not often discussed as separate processes and are typically referred to collectively as fractionation during degassing.

We calculate $\delta^{13}C$ and $\Delta^{14}C$ values as,

$$\delta^{13}C = \left(\frac{R_{sample}}{R_{std}} - 1\right) * 1000‰ \quad \text{(Eq. 7), and}$$

$$\Delta^{14}C = \left(\frac{\left({}^{14}C/_{12}C\right)_{corr}}{\left({}^{14}C/_{12}C\right)_{std} * \exp\left(\frac{2023-1950}{8267}\right)} - 1\right) * 1000‰ \quad \text{(Eq. 8), where}$$

$$\left({}^{14}C/_{12}C\right)_{corr} = \left({}^{14}C/_{12}C\right)_{sample} \left(\frac{1+\delta^{13}C_{std}/1000}{1+\delta^{13}C_{sample}/1000}\right)^2 \quad \text{(Eq. 9).}$$

Within these equations, R_{std} represents the $^{13}C/^{12}C$ ratio of the VPDB standard, and $^{14}C/^{12}C_{std}$ is 1.12E-12. Eq. 9 essentially corrects for equilibrium fractionation effects within the ^{14}C system. In this scenario and across the following sections, we assume an initial GW $\delta^{13}C_{DIC}$ value of -15‰ representing a balance of C_3 soil respiration and carbonate from calcite weathering and $\Delta^{14}C_{DIC}$ value of -500‰ representing a mix of modern soil respiration and ^{14}C-dead carbonate carbon (Table 1). We also assume that on the timescales of stream transport, radioactive decay of ^{14}C is negligible.

2.2.2 Scenario 2: Groundwater degassing with continuous CO_2 sources

In Scenario 2, we incorporate continuous inputs from groundwater inflows and stream corridor CO_2 production via respiration (Fig. 1b). In this scenario, we amend Eq. 3 to incorporate these inputs as,

$$\frac{\partial DIC}{\partial t} = -k\left(CO_{2(aq)} - CO_{2(aq)sat}\right) + Q\left(DIC_{gw} - DIC\right) + F_{prod} \quad \text{Eq. (10),}$$

where Q is the volume-normalized groundwater inflow rate (s^{-1}), and F_{prod} is the net respiration flux (mol/L/s) which represents a combination of net respiration within the water column along with hyporheic zone respiration. This method assumes that alkalinity remains constant, ignoring potential variability in groundwater inflow alkalinities, anaerobic respiration that may contribute additional alkalinity, and carbonate precipitation which would decrease alkalinity. This situation is analogous to a homogenous stream reach with active GW inputs. Similar to Scenario 1, we solve this equation using an explicit numerical scheme across discretized timesteps. The same methods are applied, whereby at each timestep, a new DIC value is calculated and the DIC system is speciated based on the Venkiteswaran et al. (2014) scheme. As above, GW is specified

with a pCO_2 of 20,000 ppm; $\delta^{13}C_{DIC}$ value of -15‰ representing a balance of C_3 soil respiration and carbonate from calcite weathering; and $\Delta^{14}C_{DIC}$ of -500‰ representing a mix of modern soil respiration and ^{14}C-dead carbonate carbon. Stream corridor respiration is assumed to have a $\delta^{13}C_{DIC}$ value of -27‰ and $\Delta^{14}C_{DIC}$ of -66‰ representing modern carbon. As in Scenario 1, we vary alkalinity across our simulations from 0 – 6 meq/L, though for simplicity we include only 0.1, 1.0, and 4.0 meq/L simulations in the main text. We also vary input flux rates as 10^{-7} (low), 10^{-6} (med), and $10^{-5.5}$ (high) mol/L/s and the ratio of input fluxes from GW versus stream corridor respiration with ratio values of 0.001 (99.9% GW), 1 (equal contributions), and 1000 (99.9% stream corridor respiration).

2.2.3 Scenario 3: Stream Network CO_2 Model

Finally, to explore the complexity of alkalinity controls on stream network-scale CO_2 and isotope dynamics, we incorporate DIC speciation reactions into an existing stream network advection-reaction model of dissolved CO_2 (Fig. 1). This model was originally developed, applied, and validated for the East River watershed in Gothic, CO, USA (Saccardi & Winnick, 2021). Briefly, the East River watershed is an 87 km^2, high elevation, mountainous watershed, with annual flow dominated by spring snowmelt (Winnick et al., 2017). In this model, we consider CO_2 fluxes from: (1) groundwater with a specified pCO_2 and inflow fluxes that scale with changes in upstream accumulating area and specified runoff values reflecting flow conditions from August, 2019; (2) hyporheic exchange parameterized using a surface renewal-theory mass-transfer model (Grant et al., 2018; Winnick, 2021) and assuming a constant offset between hyporheic zone and stream CO_2 meant to reflect net respiration; (3) water column net respiration at a specified volume-normalized rate; and (4) atmospheric exchange in which gas exchange velocities (k_{600}) are parameterized based on slope and discharge via empirical correlations between energy dissipation rates and k_{600} (Ulseth et al., 2019). The full details of model derivation and parameterization are presented in Saccardi and Winnick (2021), and the simulated map of stream pCO_2 values is shown in Fig. 1. Here, we update the model and simplify a number of model parameterizations as: (1) here, we ignore wetland contributions and assume all groundwater sources have the same pCO_2 across the watershed, as opposed to our original model which specified high pCO_2 values from wetland areas; (2) we ignore snow-plugs which were introduced into the model as zones with no atmospheric gas exchange to match field observations. For simplification, we assume a single groundwater alkalinity value for the whole watershed, and that stream-corridor respiration does not alter alkalinity, ignoring, for example, alkalinity contributions from anaerobic respiration. Finally, we update the underlying model equations to incorporate DIC speciation as,

$$\frac{\partial DIC}{\partial t} = -v\frac{\partial DIC}{\partial x} - k\left(CO_{2(aq)} - CO_{2(aq)sat}\right) + Q\left(DIC_{gw} - DIC\right) + F_{wc} + k_{hz} * C_{hz} \qquad \text{Eq. (11)},$$

where v is advection velocity (m/s), x is distance along stream (m), F_{wc} is the water column net respiration flux ($ER - GPP$; mol/L/s), k_{hz} is the rate of hyporheic exchange (s^{-1}), and C_{hz} is the offset between stream and hyporheic zone DIC (mol/L). This model is applied to NHD HR streamlines at sub-reach scales. In this model exercise, we assume steady-state conditions (e.g. $\partial DIC/\partial t = 0$), and use a backwards-difference method to solve for changes in DIC spatially across the stream network. At each new downstream spatial grid, we then use the updated DIC

and specified alkalinity value to speciate the DIC system. For modeled cells, we discretize NHD HR stream flowlines at a 0.5 m spacing.

We solve the model separately for three alkalinity values: 0, 1 (roughly the average measured site alkalinity), and 4 meq/L. We assume groundwater pCO_2 of 20,000 ppm in the range of measured soil values (Winnick et al., 2020), an elevation of hyporheic zone pCO_2 above stream values of 700 ppm, and an F_{wc} value of 10^{-9} mol/L/s, roughly aligning with optimized values from the model validation of Saccardi and Winnick (2021). Crucially, our intent here is not to validate the model against previous field observations, but instead to interrogate how the carbonate buffering dynamics explored in the idealized Scenario's 1 and 2 may be reflected in real-world systems. Given previous studies which have shown the importance of carbonate weathering for generating alkalinity within the East River system (Carroll et al., 2018; Winnick et al., 2017), we assume end-member isotope compositions from Scenario 2, shown in Table 1.

3. Results

3.1 Scenario 1 Results

The temporal evolution of pCO_2, $\delta^{13}C_{DIC}$, and $\Delta^{14}C_{DIC}$ for our groundwater degassing simulations are shown in Fig. 2 across a range of alkalinities. Within these plots, the time axis (t^*) is non-dimensional, representing the simulation time (s) multiplied by the specified reaeration rate (s^{-1}); these values are also equivalent to non-dimensional distance, and simulation time could be scaled to a dimensional distance by multiplying by an advective velocity. As shown in the top panel, high initial GW pCO_2 values equilibrate with atmospheric values over t^* timescales of ~5-40 (unitless). Higher alkalinity values result in slightly longer equilibration timescales, as highlighted by the inset, though values eventually approach the same atmospheric pCO_2 levels. This increase in equilibration timescale is controlled by carbonate buffering reactions which act to resupply CO_2 as degassing progresses as discussed in Section 1. These changes in equilibration timescales due to carbonate buffering are relatively muted as compared to isotopic equilibration.

In Fig. 2b, $\delta^{13}C_{DIC}$ starts at GW values of -15‰ and approach equilibrium with atmospheric $\delta^{13}C_{CO2}$ values of -9‰ through time. Importantly, the final equilibrated $\delta^{13}C_{DIC}$ values vary as a function of alkalinity. Under low alkalinity conditions, atmosphere-equilibrated $CO_{2(aq)}$ represents the primary component of DIC, and $\delta^{13}C_{DIC}$ values approach atmospheric values of -9‰. Notably, under no alkalinity conditions, $\delta^{13}C_{DIC}$ is slightly elevated above atmospheric as CO_2 is only ~84% of total DIC. Under high alkalinity conditions, the primary form of DIC is as HCO_3^- or CO_3^{2-}, which due to equilibrium fractionation are elevated ~9‰ above $CO_{2(aq)}$ values; thus, the DIC pool approaches ~0‰ when equilibrated with the atmosphere. In addition to these changes in final equilibrated values, alkalinity also strongly impacts the timescales of equilibration. Under zero alkalinity conditions, isotopic equilibration timescales are comparable to those of pCO_2. As alkalinity increases, however, $\delta^{13}C_{DIC}$ equilibration timescales increase significantly, with the high alkalinity (6 meq/L) scenario requiring non-dimensional timescales of >1000 as compared to CO_2 equilibration timescales of >10.

Values of $\Delta^{14}C_{DIC}$ display similar patterns with a few important differences. First, alkalinity has no impact on final $\Delta^{14}C_{DIC}$ values, as the associated equilibrium fractionation is normalized for within Eq. 9. However, as equilibrium fractionation is roughly twice as large for ^{14}C as ^{13}C, a larger initial proportion of ^{14}C is buffered within the HCO_3^- + CO_3^{2-} DIC pool; thus, timescales of equilibration are slightly larger.

In Figure 3, we directly evaluate these timescales of equilibration through the calculation of folding-times of $\boldsymbol{\tau}^{99}$, $\boldsymbol{\tau}^{90}$, and $\boldsymbol{\tau}^{e}$ representing the non-dimensional time required to degas 99%, 90%, and ~46% of GW CO_2, respectively. Figure 3a shows the factor increase in each of these timescales for a given alkalinity compared to a simulation with no alkalinity. Alkalinity has relatively little impact on the $\boldsymbol{\tau}^{90}$ and $\boldsymbol{\tau}^{e}$ timescales, though it causes an increase of over 2.5x in $\boldsymbol{\tau}^{99}$ in the high alkalinity simulation. Given the nature of our non-dimensional analysis, this factor increase is a scalable result. In other words, for any given combination of reaeration rates, stream velocities, and initial pCO_2 values, this would result in a 2.5x increase in the distance over which a groundwater seep degassed 99% of its CO_2. Physically, this sensitivity of $\boldsymbol{\tau}^{99}$ values demonstrates that the impact of carbonate buffering is highest at near-atmospheric pCO_2, resulting in longer timescales to lose the final 1% of pCO_2. This is visually evident in Figure 2a as the alkalinity curves diverge only as they approach atmospheric values.

The ratio of isotopic equilibration timescales to pCO_2 equilibration is shown in 3b. Increases in alkalinity result in roughly linear increases in the ratio of these equilibration timescales for $\boldsymbol{\tau}^{90}$ and $\boldsymbol{\tau}^{e}$. In contrast, $\boldsymbol{\tau}^{99}$ values plateau above an alkalinity of ~4 meq/L. Importantly, the impacts on equilibration timescales are very similar between $\delta^{13}C_{DIC}$ and $\Delta^{14}C_{DIC}$, with small variations due to differing equilibrium fractionation factors that result in slight differences in the proportion of ^{13}C v. ^{14}C buffered by the HCO_3^- and CO_3^{2-} pools.

Lastly for Scenario 1, we calculate the proportion of CO_2 emissions supported by carbonate buffering across a range of alkalinity and GW pCO_2 values, shown in Figure 4. This value is calculated by subtracting the total loss of $CO_{2(aq)}$ during atmospheric equilibration from total DIC loss during equilibration, normalized by the total DIC loss. Carbonate buffering plays a negligible role in CO_2 emissions when alkalinity is low and GW pCO_2 is high, as both of these conditions result in a smaller proportional storage of CO_2 as HCO_3^- + H^+. However, under conditions of high alkalinity and low GW pCO_2, carbonate buffering may account for up to 90% of emissions across the alkalinity and pCO_2 values tested. We note that these estimates assume no calcite precipitation. This may become an important factor in high alkalinity systems with available Ca^{2+}, whereby degassing raises the calcite saturation state leading to mineral precipitation and further buffering of $CO_{2(aq)}$ concentrations.

3.2 Scenario 2 Results

In Scenario 2, we incorporate continuous GW and net stream corridor respiration fluxes during seep degassing, reflecting more realistic scenarios in which evasion fluxes are partially supported by localized CO_2 sources. The temporal patterns of pCO_2, $\delta^{13}C_{DIC}$, and $\Delta^{14}C_{DIC}$ are shown in Figure 5 across a range of alkalinities, total CO_2 source fluxes, and ratios of GW to stream corridor sources. Across Figure 4a-c, pCO_2 displays similar patterns to Figure 2. As total CO_2 sources increase, steady-state pCO_2 values increase to well above atmosphere-equilibrated

values. These elevated pCO_2 values represent a stable balance between specific input fluxes and evasion rates, which can be calculated by assuming steady-state (dC/dt = 0) and rearranging Eq. 10 as,

$$CO_{2(aq)steady-state} = \frac{Q(DIC_{gw}-DIC)+F_{prod}}{k} + CO_{2(aq)sat} \quad \text{Eq (12).}$$

As steady-state pCO_2 values increase, the effects of alkalinity on degassing patterns becomes more muted. For example, in Figure 4c, there is little visible difference between the high alkalinity simulation (4 meq/L) and the low alkalinity simulation (0.1 meq/L). This demonstrates similar patterns as in Figure 3a, which shows that the impacts of equilibration timescales are relatively insignificant when evaluated at pCO_2 levels above atmospheric (i.e. $\boldsymbol{\tau}^{90}$ and $\boldsymbol{\tau}^{e}$). Patterns of pCO_2 are not impacted by the partitioning of fluxes between GW and stream corridor sources, assuming the total fluxes are the same.

Carbon isotope patterns become more complicated when considering multiple sources of different compositions. This is most clear for $\delta^{13}C_{DIC}$ where atmospheric, GW, and stream corridor respiration all have different sources, versus $\Delta^{14}C_{DIC}$ where stream corridor and atmospheric sources are roughly the same. Broadly, and as demonstrated in Scenario 1, increased alkalinity results in increasing equilibration timescales or, in this case, steady-state timescales for both $\delta^{13}C_{DIC}$ and $\Delta^{14}C_{DIC}$. These steady-state timescales are not significantly impacted by the magnitude of CO_2 source fluxes or their partitioning between GW and stream corridor respiration (i.e. comparing the yellow lines within and across the panels). Alkalinity also impacts the final steady-state value of $\delta^{13}C_{DIC}$ for a given CO_2 source flux and partitioning ratio (i.e. comparing the solid purple curve to the solid yellow curve within a panel), such that low alkalinity results in a lower $\delta^{13}C_{DIC}$ value for a given flux and partitioning ratio of carbon inputs.

Across these simulations, steady-state $\delta^{13}C_{DIC}$ and $\Delta^{14}C_{DIC}$ are also highly sensitive to both the magnitude of total source fluxes and their partitioning between GW and stream corridor sources. In the case of $\delta^{13}C_{DIC}$, as both GW and stream corridor sources have lower-than-atmospheric values, increasing CO_2 input fluxes results in a decrease in steady-state values. Further, as $\delta^{13}C_{DIC}$ of stream corridor sources are lower than GW (-27‰ v. -15‰ in these simulations), a higher proportion of stream corridor sources results in lower steady-state $\delta^{13}C_{DIC}$ values. Comparing across Figure 5d-f, we note a significant degree of equifinality in steady-state $\delta^{13}C_{DIC}$ values, whereby different combinations of alkalinity, total CO_2 sources, and source partitioning can result in similar steady-state $\delta^{13}C_{DIC}$ values. Even if alkalinity is constrained, different combinations of CO_2 sources with different $\delta^{13}C_{DIC}$ end-member values can result in the same steady-state $\delta^{13}C_{DIC}$; for example, comparing the 1.0 meq/L All Stream corridor line (green solid) in Figure 5e with the 1.0 meq/L Equal GW and Stream corridor line (green dashed) in Figure 5f.

The controls of sources on steady-state values are more easily discernible in the $\Delta^{14}C_{DIC}$ data, where values are not sensitive to alkalinity. As we set $\Delta^{14}C_{DIC}$ values of stream corridor respiration to near-atmospheric, stream corridor respiration does not have a significant impact on $\Delta^{14}C_{DIC}$ steady-state values (i.e. comparing the solid lines across panels g-i). Instead, variability is controlled by the total magnitude of GW CO_2 fluxes, which act as a source of low $\Delta^{14}C_{DIC}$ and draw down steady-state values.

3.3 Scenario 3 Results

Our previous work evaluated the controls on spatial CO_2 patterns across the East River watershed, CO_2 through comparisons of model simulations and field observations (Saccardi and Winnick, 2021). In this exercise, we compare the results of those simulations, which only represented the CO_2 component of the DIC system (equivalent to a situation with an alkalinity of 0), with our updated model. Spatial patterns of CO_2 are shown in the Supplement (SFig.'s 1,3,4) and do not result in significant visual differences in spatial patterns across the watershed as depicted in the inset of Figure 1c. In contrast to our degassing experiments in Scenarios 1 and 2, the full watershed simulation features areas in which pCO_2 increases due to inputs (GW and stream corridor respiration) that are locally higher than evasion fluxes. Under these conditions, the inclusion of alkalinity results in lower pCO_2 estimates as a proportion of CO_2 inputs is stored as $HCO_3^- + H^+$. This behavior is equivalent to temporal hysteresis modelled in Stets et al. (2017) for diel metabolic patterns, where CO_2 buildup at night is slower than O_2 depletion. At the watershed scale, there are a comparable number of model cells in which the inclusion of alkalinity results in lower as higher pCO_2 relative to no alkalinity (Fig. 7a), with a range of -53 – 34 ppm in our 1 meq/L alkalinity simulation. This range increases with increasing alkalinity (SFig.'s 2,5), but the overall pattern is unchanged.

We demonstrate the primary role of reaeration rate on whether alkalinity results in an increase or decrease in pCO_2 through its control on pCO_2 buildup versus degassing in Fig. 7b. Here, box plots of model differences for the 1 meq/L simulation are binned by the log of gas exchange velocity. Under low gas exchange velocities, the alkalinity model predicts lower pCO_2 values as the buildup of pCO_2 results in increased CO_2 'storage', and only under high gas exchange velocities does the alkalinity model predict higher pCO_2 values, equivalent patterns observed in Scenario 1. Patterns in model differences are minimal when compared across stream scale, as defined by Strahler Order in Figure 7c. There is a slight trend towards lower alkalinity model predictions at larger stream scales, and this likely reflects the flatter topography and lower gas exchange velocities in the higher order streams. Averaged across the watershed, the alkalinity model predicts slightly lower pCO_2 values by -0.054 ppm. Counterintuitively, total watershed evasion fluxes from the alkalinity model are slightly higher, due to outsized flux contributions from areas with high gas exchange velocities (where the alkalinity model predicts slightly higher pCO_2) on total fluxes. The difference in total watershed fluxes reflects the additional CO_2 stored as $HCO_3^- + H^+$ in exfiltrating groundwater, as both simulations are given the same GW pCO_2 and feature the same total stream corridor respiration fluxes.

We also show how carbonate buffering reactions impact relationships between pCO_2 and $\delta^{13}C_{DIC}$ in Fig. 8 for the East River with an alkalinity of 1 meq/L, which expands on Fig. 5a by incorporating stream corridor respiration sources and scenarios with both increasing and decreasing pCO_2. During GW degassing in the headwaters, patterns resemble the degassing experiments from Scenario 1. However, in downstream reaches where pCO_2 experiences local variability in response to changing balances between input fluxes and evasion rates, model output deviates significantly from the degassing patterns. When local sources act to increase pCO_2, the total amount of DIC added is relatively small compared to the existing pool; thus, $\delta^{13}C_{DIC}$ is largely insensitive to changes in pCO_2. This behavior is highlighted in the inset in Fig.

8, in which local changes in pCO_2 result in minimal $\delta^{13}C_{DIC}$ changes, and overall patterns feature no large-scale co-variability. We note that this decoupling occurs in spite of the fact that lower $\delta^{13}C_{DIC}$ values of stream corridor respiration relative to GW are acting to drive steeper, more sensitive correlations between pCO_2 and $\delta^{13}C_{DIC}$. This decoupling of pCO_2 and $\delta^{13}C_{DIC}$ is similar with higher alkalinity (SFig 6) and is also significant even in low alkalinity conditions of 0.1 meq/L (SFig 7). These results show that even under low alkalinity, pCO_2 and $\delta^{13}C_{DIC}$ do not covary systematically across the watershed scale except during initial GW degassing.

To demonstrate the potential use of paired $\delta^{13}C_{DIC}$ and $\Delta^{14}C_{DIC}$ in evaluating local partitioning between GW and stream corridor sources of DIC, we plot data from each model cell of the 1 meq/L simulation in $\delta^{13}C_{DIC}$ v. $\Delta^{14}C_{DIC}$ space in Figure 9a. Contour lines represent degassing patterns for an initial DIC pool representing the isotopic end-member composition of varying mixtures of GW and stream corridor sources, generated using the same methods of Scenario 1. We note that while this plot resembles an end-member mixing model, there is some curvature in the contour lines that reflect slight differences in the timescales of equilibration for ^{14}C v. ^{13}C discussed above. As shown, 1st order streams largely fall along All-GW degassing contour lines to start with shift towards higher contributions from stream corridor respiration as values approach atmospheric equilibration. In general, there is a trend towards higher stream corridor respiration contributions at higher stream order, with a significant degree of variability within each order. We show this directly in Figure 9b, where the % GW contribution to DIC is calculated using a nearest-neighbor function to find which contour line passes through each model output point. Across all model cells, GW contributions vary from 100 – 4%. We simulate a consistent transition from GW to stream corridor DIC sources at larger network scales, with the switch from GW to stream corridor dominance occurring between 2nd and 3rd order streams, consistent with our previous modeling results (Saccardi & Winnick, 2021). We note that output from the 4.0 meq/L simulation results in a shift towards higher GW contributions across the watershed, as GW has a significantly larger DIC concentration than the 1.0 meq/L simulation (SFig 8).

4. Discussion

4.1 Alkalinity controls on CO_2 concentrations and fluxes

Across the simulated scenarios, we demonstrate quantitatively how alkalinity acts to alter the equilibration of dissolved CO_2 with the atmosphere in rivers and streams. Increased alkalinity, as previously hypothesized, increases the role of carbonate buffering reactions to maintain pCO_2 along the stream reach. During active degassing, as shown in Scenarios 1-3, carbonate buffering reactions result in minimally increased atmosphere equilibration timescales, acting to maintain slightly elevated pCO_2. Notably, however, these timescale increases are minimal and are only in evidence at near-atmospheric pCO_2 values. Further, under conditions in which dissolved CO_2 is actively building up, for example when local rates of stream corridor respiration are higher than degassing rates, carbonate buffering maintains lower pCO_2 concentrations as it actively stores CO_2 as $HCO_3^- + H^+$. This effect is equivalent to the Revelle factor often discussed in the oceanography literature (Broecker et al., 1979; Revelle & Suess, 1957), and has been shown to impact stream CO_2 fluxes (Wang et al., 2021).

In a compilation of US stream data, Stets et al. (2017) show that systems with high alkalinity tend to exhibit higher pCO_2 at moderate stream scales (discharge of 0.1 – 6 m^3/s) than systems with low alkalinity. This was hypothesized to reflect carbonate buffering reactions, through their role in maintaining high pCO_2 during downstream degassing. In our modeling exercises, we show that carbonate buffering is unable to explain these observed patterns. In fact, when simulating at the stream network scale, we find that carbonate buffering reactions result in the opposite pattern as observed in the Stets et al. compilation: pCO_2 is slightly elevated in first order streams but is typically lower in 3rd-5th order streams when alkalinity is included, reflecting the increasing importance of stream corridor respiration sources and lower gas exchange velocities that allow generated CO_2 to be stored as $HCO_3^= + H^+$ (Fig. 8b).

While beyond the scope of our study, we tentatively suggest that if the observational patterns presented in Stets et al. (2017) are robust, they likely reflect either systematically higher source fluxes (GW inputs and/or stream corridor respiration) or systematically lower gas exchange velocities potentially reflecting lower topographic relief (e.g. Rocher-Ros et al., 2019). Regarding elevated source fluxes, we note that Stets et al. (2017) demonstrate lower *p*CO2 in the smallest high alkalinity streams which would suggest lower GW pCO_2 sources, and we are unaware of a mechanism that would link high alkalinity with higher stream corridor respiration rates. In terms of topography, as high alkalinity typically reflects increased chemical weathering rates often associated with soluble minerals such as carbonates, these landscapes may preferentially exhibit lower gas exchange velocities in higher order streams, resulting in elevated pCO_2 at larger stream scales. To test this hypothesis would require local flow and topographic data, which are not included in the original compilation, and future work is required to test this hypothesis. We also note that our stream network model simulations, in which the only altered variable is alkalinity, are not directly comparable to the US compilation data. For example, we hold GW pCO_2 constant, whereas increased alkalinity may be expected to co-occur with reduced GW pCO_2 based on chemical weathering reactions (e.g. Winnick & Maher, 2018).

We also demonstrate that increasing alkalinity and decreasing GW pCO_2 values result in increasing relative contributions of carbonate buffering to total degassing fluxes (Fig. 4). Under conditions where GW is the sole source of stream pCO_2, carbonate buffering may account for >60% of total degassing fluxes when GW has high alkalinity (>4 meq/L) and relatively moderate pCO_2 (<5000 ppm). These values are consistent with findings in Duvert et al. (2019), where carbonate buffering reactions were shown to support as much as ~60% of total fluxes in a high alkalinity, tropical stream system. While not included in our Fig. 4 analysis, carbonate buffering contributions to total fluxes would also decrease with increasing stream corridor respiration. Taken together, these findings highlight the importance of accounting for carbonate buffering reactions in budgeting stream network CO_2 fluxes, particularly in high alkalinity (>1 meq/L) systems.

4.2 Alkalinity impacts on carbon isotope source partitioning

In contrast to the effects on CO_2 equilibration timescales, carbonate buffering reactions lead to much longer isotope equilibration timescales for both $\delta^{13}C_{DIC}$ and $\Delta^{14}C_{DIC}$. Mechanistically, this is due to the fact that pCO_2 is only buffered by the proportion of HCO_3^- that does not contribute to alkalinity (CO_2 stored as $HCO_3^- + H^+$). In contrast, the isotopic ratio of DIC is buffered by the

entire HCO_3^- and CO_3^{2-} pools, which under high alkalinity are much larger than the CO_2 pool that is actively degassing. As the equilibration timescales for both are regulated by the gas exchange velocity, this larger isotopic buffering results in a much longer equilibration timescale. For example, at an alkalinity of 1 meq/L and initial GW pCO_2 of 20,000 ppm, the CO_2 stored as HCO_3^-+ H^+ is 1.3% the size of the $CO_{2(aq)}$ pool, whereas the full buffering pool of ^{12}C, ^{13}C, and ^{14}C encapsulated in HCO_3^- + CO_3^{2-} is 150% the size of the $CO_{2(aq)}$ pool. This difference is amplified by the fact that gas exchange rates, and thus isotope equilibration rates, slow significantly as pCO_2 approaches atmospheric values. Further, a higher proportion of total ^{13}C and ^{14}C are contained within HCO_3^- and CO_3^{2-} relative to ^{12}C due to equilibrium fractionation within the DIC pool. Thus, high alkalinity is more effective at buffering the isotopic composition of DIC, which under high alkalinity conditions does not equilibrate until almost all of the net CO_2 degassing has already occurred. At the stream network scale, this results in stream $\delta^{13}C_{DIC}$ and $\Delta^{14}C_{DIC}$ that are much less sensitive to sub-reach changes in topography and source inputs that can dramatically alter pCO_2 over small scales. While these results have been demonstrated indirectly through the application of similar models to groundwater degassing (e.g. Venkitaswaren et al., 2017), this study is the first to identify and quantify these timescales for both $\delta^{13}C_{DIC}$ and $\Delta^{14}C_{DIC}$.

These differences in the magnitude impacts of buffering dynamics on pCO_2 versus carbon isotopes greatly complicates methods of CO_2 source evaluation. The size of the isotope buffering pool effectively acts to decouple variations between carbon concentrations (pCO_2 or DIC) and isotopic composition ($\delta^{13}C_{DIC}$ or $\Delta^{14}C_{DIC}$). During degassing, the bulk of isotopic change occurs after pCO_2 has equilibrated with the atmosphere, which makes measurements of covariation analytically difficult. More importantly, in situations where CO_2 (and DIC) is building up rather than degassing, $\delta^{13}C_{DIC}$ or $\Delta^{14}C_{DIC}$ are largely insensitive to these new inputs. This results in reach-scale patterns in which $\delta^{13}C_{DIC}$ and pCO_2 are largely decoupled and deviate significantly from the overall degassing pattern, as shown in Fig. 8. Typical isotopic source evaluation methods either employ linear mixing models of pCO_2 or DIC and $\delta^{13}C_{DIC}$ (e.g. Campeau et al., 2017, 2018) or degassing models (Venkiteswaran et al., 2014). The assumptions underlying both of these methods is that pCO_2 and $\delta^{13}C_{DIC}$ co-vary systematically across a given study area. We show that this is not the case; carbonate buffering acts to decouple pCO_2 and $\delta^{13}C_{DIC}$ patterns in all but the 1st order headwaters which are dominated by GW degassing. This decoupling occurs even at low and moderate alkalinity values (0.1 meq/L shown in SFig 7; 1 meq/L shown in Fig. 8). Therefore, studies that utilize pCO_2- or DIC- $\delta^{13}C_{DIC}$ methods for evaluating carbon sources are only accurate under very low alkalinity conditions or in directly evaluating GW degassing trends in spring-fed headwaters.

Despite the factors that complicate relationships between isotope composition and pCO_2, our modeling simulations suggest a useful path forward. Specifically, $\delta^{13}C_{DIC}$ and $\Delta^{14}C_{DIC}$ both represent the full DIC pool and have equilibration timescales that are similarly impacted by alkalinity. Therefore, they may be used to more directly partition DIC sources through end-member mixing analyses. Further, the increased equilibration timescales in high alkalinity systems mean that point measurements of $\delta^{13}C_{DIC}$ and $\Delta^{14}C_{DIC}$ are more integrative of upstream conditions and may provide useful insight into broader spatial trends than pCO_2, which can often vary over scales of 10's of meters (e.g. Johnson et al., 2008). Paired $\delta^{13}C_{DIC}$ and $\Delta^{14}C_{DIC}$ measurements may be particularly useful for DIC source partitioning in systems where

groundwater DIC is controlled by carbonate mineral weathering reactions, such as watersheds with limestone or shale bedrock. Under these conditions and as parameterized across our simulations, GW, stream corridor respiration, and the atmosphere all represent unique end-members in $\delta^{13}C_{DIC}$- $\Delta^{14}C_{DIC}$ space (e.g. Table 1). We note that Sveinbjörnsdóttir et al. (2020) have previously employed paired $\delta^{13}C_{DIC}$- $\Delta^{14}C_{DIC}$ to evaluate DIC sources; however, they used a linear end-member mixing model, which our results show neglects non-linear variations between $\delta^{13}C_{DIC}$ and $\Delta^{14}C_{DIC}$ degassing rates and may therefore only be accurate under low alkalinity conditions.

In our simulations, we calculate the contributions of GW versus stream corridor respiration to DIC using simulated $\delta^{13}C_{DIC}$- $\Delta^{14}C_{DIC}$ relationships. At any given simulated stream point, measured values are representing the integration of upstream processes at spatial scales dependent on stream velocity, gas exchange velocity, and the alkalinity-dependent equilibration timescales of carbon isotope values. We propose that these methods may be employed within field systems, which requires the characterization of end-member source $\delta^{13}C_{DIC}$- $\Delta^{14}C_{DIC}$ values, along with alkalinity measurements to calculate contour mixing lines (see Supplemental Material for example code). Currently, methods for estimating source contributions within a stream reach are intensive, and typically involve calculating stream corridor metabolic rates through DO sensor deployment and absolute CO_2 fluxes through high resolution sampling (e.g. (Hotchkiss et al., 2015). While $\Delta^{14}C_{DIC}$ measurements are costly, this method has the advantage of allowing for rapid characterization of source partitioning across watershed scales, through sampling campaigns that target multiple streams. Traditionally, source characterization across stream orders within a watershed would require redeployment of DO sensors at each new reach; whereas, this method would only require taking additional samples at each reach assuming relatively consistent end-member sources across the watershed.

4.3 Model Limitations

While these models are meant to be broadly representative of the processes controlling atmospheric equilibration of river and stream waters, there are a number of assumptions we have made that must be validated on a site-by-site basis for direct data comparisons. First, our simulations parameterize stream corridor metabolism as net respiration rather than separately simulating photosynthesis and respiration. This parameterization assumes that organic matter derived from terrestrial materials is the same as that synthesized in the stream, such that stream corridor photosynthesis and respiration have equal and opposite impacts on isotopic composition. This assumption may be violated, for example, in sites where terrestrially-derived DOC represents C_4 plant matter, and at the field-scale, measurements of distinct isotopic end-member for different DOC sources are needed to evaluate this assumption. As stated throughout the manuscript, we also neglect processes that alter alkalinity concentrations, which may include anaerobic respiration, calcite precipitation, and spatiotemporal changes in GW chemistry. We similarly neglect CO_2 generation from methane oxidation that may result in distinctly low $\delta^{13}C_{DIC}$ values. Lastly, we assume that there is no kinetic fractionation associated with CO_2 degassing from turbulent exchange, and that apparent fractionation during degassing reflects only equilibration with the elevated atmospheric values of $\delta^{13}C_{DIC}$ and $\Delta^{14}C_{DIC}$. We feel that this issue remains an open question that has not been directly addressed in stream environments,

659 though our modeling framework is flexible to incorporate it as a specified kinetic fractionation
660 factor when molecular diffusion is a significant factor in degassing rates.
661
662 **5. Conclusions**
663 Given the recent recognition of carbonate buffering reactions as an important control on spatial
664 patterns of CO_2 concentrations and fluxes in stream systems, we develop a non-dimensional
665 reactive transport framework for evaluating their impacts on atmospheric equilibration of
666 dissolved inorganic carbon. We find that while carbonate buffering does increase the timescales
667 over which pCO_2 approaches steady-state values, these changes are relatively small and cannot
668 explain observations of elevated pCO_2 at increasing spatial scales in high alkalinity versus low
669 alkalinity systems. This increase in equilibration timescale, along with increased contributions of
670 carbonate buffering reactions to total CO_2 fluxes, depends on the size of the buffering reservoir
671 (or amount of CO_2 stored as $HCO_3^- + H^+$) relative to $CO_{2(aq)}$, such that carbonate buffering
672 reactions contribute a larger proportion of CO_2 fluxes as alkalinity increases and GW pCO_2
673 decreases. In contrast to CO_2, the isotopic composition of DIC is buffered by the entire DIC pool
674 as CO_2 equilibrates with the atmosphere, which is much larger than the pool of CO_2 stored as
675 $HCO_3^- + H^+$. As a result, isotopic equilibration timescales are much more sensitive to stream
676 alkalinity, with $\delta^{13}C_{DIC}$ and $\Delta^{14}C_{DIC}$ increasing by ~2 orders of magnitude relative to CO_2
677 timescales. The result of this mismatch in timescales is that under moderate alkalinity conditions,
678 isotope composition becomes largely decoupled from pCO_2, rendering typical methods for CO_2
679 source tracing ineffective. We show, however, that due to similar impacts on equilibration
680 timescales, paired $\delta^{13}C_{DIC}$ and $\Delta^{14}C_{DIC}$ measurements may be effective tracers of GW versus
681 stream corridor respiration sources of DIC in environments where GW DIC is controlled by
682 carbonate weathering reactions, typical of moderate to high alkalinity systems. Taken together,
683 we present a generalizable framework for quantifying and interpreting the role of carbonate
684 buffering reactions on stream CO_2 dynamics and develop a new potential method for utilizing the
685 isotopic composition of DIC to trace stream carbon sources.
686
687 **Acknowledgements**
688 We thank Stephen Burns and Berry Williams for useful discussions about the carbon isotope
689 modelling. This work was supported by the National Science Foundation (EAR-2103520 to
690 MJW).
691

692 **Data Availability Statement**

693 All code used in this work is available in the Supplemental Information. We will also make all
694 code available publicly via the open-source Hydroshare platform following the first round of
695 review.
696
697 **References**
698 Broecker, W. S., Takahashi, T., Simpson, H. J., & Peng, T.-H. (1979). Fate of Fossil Fuel
699 Carbon Dioxide and the Global Carbon Budget. *Science*, *206*(4417), 409–418.
700 https://doi.org/10.1126/science.206.4417.409

Campeau, A., Bishop, K., Nilsson, M. B., Klemedtsson, L., Laudon, H., Leith, F. I., Öquist, M., & Wallin, M. B. (2018). Stable Carbon Isotopes Reveal Soil-Stream DIC Linkages in Contrasting Headwater Catchments. *Journal of Geophysical Research: Biogeosciences*, *123*(1), 149–167. https://doi.org/10.1002/2017JG004083

Campeau, A., Wallin, M. B., Giesler, R., Löfgren, S., Mörth, C.-M., Schiff, S., Venkiteswaran, J. J., & Bishop, K. (2017). Multiple sources and sinks of dissolved inorganic carbon across Swedish streams, refocusing the lens of stable C isotopes. *Scientific Reports*, *7*(1), Article 1. https://doi.org/10.1038/s41598-017-09049-9

Carroll, R. W. H., Bearup, L. A., Brown, W., Dong, W., Bill, M., & Willlams, K. H. (2018). Factors controlling seasonal groundwater and solute flux from snow-dominated basins. *Hydrological Processes*, *32*(14), 2187–2202. https://doi.org/10.1002/hyp.13151

Cole, J. J., Prairie, Y. T., Caraco, N. F., McDowell, W. H., Tranvik, L. J., Striegl, R. G., Duarte, C. M., Kortelainen, P., Downing, J. A., Middelburg, J. J., & Melack, J. (2007). Plumbing the Global Carbon Cycle: Integrating Inland Waters into the Terrestrial Carbon Budget. *Ecosystems*, *10*(1), 172–185. https://doi.org/10.1007/s10021-006-9013-8

Cole, T. L., Torres, M. A., & Kemeny, P. C. (2022). The Hydrochemical Signature of Incongruent Weathering in Iceland. *Journal of Geophysical Research: Earth Surface*, *127*(6), e2021JF006450. https://doi.org/10.1029/2021JF006450

DelSontro, T., Beaulieu, J. J., & Downing, J. A. (2018). Greenhouse gas emissions from lakes and impoundments: Upscaling in the face of global change. *Limnology and Oceanography Letters*, *3*(3), 64–75. https://doi.org/10.1002/lol2.10073

722 Drake, T. W., Raymond, P. A., & Spencer, R. G. M. (2018). Terrestrial carbon inputs to inland
723 waters: A current synthesis of estimates and uncertainty. *Limnology and Oceanography*
724 *Letters*, *3*(3), 132–142. https://doi.org/10.1002/lol2.10055
725 Druhan, J. L., Guillon, S., Lincker, M., & Arora, B. (2021). Stable and radioactive carbon
726 isotope partitioning in soils and saturated systems: A reactive transport modeling
727 benchmark study. *Computational Geosciences*, *25*(4), 1393–1403.
728 https://doi.org/10.1007/s10596-020-09937-6
729 Duvert, C., Bossa, M., Tyler, K. J., Wynn, J. G., Munksgaard, N. C., Bird, M. I., Setterfield, S.
730 A., & Hutley, L. B. (2019). Groundwater-Derived DIC and Carbonate Buffering Enhance
731 Fluvial CO2 Evasion in Two Australian Tropical Rivers. *Journal of Geophysical*
732 *Research: Biogeosciences*, *124*(2), 312–327. https://doi.org/10.1029/2018JG004912
733 Friedlingstein, P., O'Sullivan, M., Jones, M. W., Andrew, R. M., Gregor, L., Hauck, J., Le
734 Quéré, C., Luijkx, I. T., Olsen, A., Peters, G. P., Peters, W., Pongratz, J., Schwingshackl,
735 C., Sitch, S., Canadell, J. G., Ciais, P., Jackson, R. B., Alin, S. R., Alkama, R., … Zheng,
736 B. (2022). Global Carbon Budget 2022. *Earth System Science Data*, *14*(11), 4811–4900.
737 https://doi.org/10.5194/essd-14-4811-2022
738 Gómez-Gener, L., Rocher-Ros, G., Battin, T., Cohen, M. J., Dalmagro, H. J., Dinsmore, K. J.,
739 Drake, T. W., Duvert, C., Enrich-Prast, A., Horgby, Å., Johnson, M. S., Kirk, L.,
740 Machado-Silva, F., Marzolf, N. S., McDowell, M. J., McDowell, W. H., Miettinen, H.,
741 Ojala, A. K., Peter, H., … Sponseller, R. A. (2021). Global carbon dioxide efflux from
742 rivers enhanced by high nocturnal emissions. *Nature Geoscience*, *14*(5), Article 5.
743 https://doi.org/10.1038/s41561-021-00722-3

744 Grant, S. B., Azizian, M., Cook, P., Boano, F., & Rippy, M. A. (2018). Factoring stream
745 turbulence into global assessments of nitrogen pollution. *Science*, *359*(6381), 1266–1269.
746 https://doi.org/10.1126/science.aap8074
747 Hotchkiss, E. R., Hall Jr, R. O., Sponseller, R. A., Butman, D., Klaminder, J., Laudon, H.,
748 Rosvall, M., & Karlsson, J. (2015). Sources of and processes controlling CO2 emissions
749 change with the size of streams and rivers. *Nature Geoscience*, *8*(9), Article 9.
750 https://doi.org/10.1038/ngeo2507
751 Johnson, M. S., Lehmann, J., Riha, S. J., Krusche, A. V., Richey, J. E., Ometto, J. P. H. B., &
752 Couto, E. G. (2008). CO2 efflux from Amazonian headwater streams represents a
753 significant fate for deep soil respiration. *Geophysical Research Letters*, *35*(17).
754 https://doi.org/10.1029/2008GL034619
755 Kirk, L., & Cohen, M. J. (2023). River Corridor Sources Dominate CO2 Emissions From a
756 Lowland River Network. *Journal of Geophysical Research: Biogeosciences*, *128*(1),
757 e2022JG006954. https://doi.org/10.1029/2022JG006954
758 Lauerwald, R., Allen, G. H., Deemer, B. R., Liu, S., Maavara, T., Raymond, P., Alcott, L.,
759 Bastviken, D., Hastie, A., Holgerson, M. A., Johnson, M. S., Lehner, B., Lin, P.,
760 Marzadri, A., Ran, L., Tian, H., Yang, X., Yao, Y., & Regnier, P. (n.d.). Inland water
761 greenhouse gas budgets for RECCAP2: 2. Regionalization and homogenization of
762 estimates. *Global Biogeochemical Cycles*, *n/a*(n/a), e2022GB007658.
763 https://doi.org/10.1029/2022GB007658
764 Polsenaere, P., & Abril, G. (2012). Modelling CO2 degassing from small acidic rivers using
765 water pCO2, DIC and δ13C-DIC data. *Geochimica et Cosmochimica Acta*, *91*, 220–239.
766 https://doi.org/10.1016/j.gca.2012.05.030

767 Raymond, P. A., Hartmann, J., Lauerwald, R., Sobek, S., McDonald, C., Hoover, M., Butman,
768 D., Striegl, R., Mayorga, E., Humborg, C., Kortelainen, P., Dürr, H., Meybeck, M., Ciais,
769 P., & Guth, P. (2013). Global carbon dioxide emissions from inland waters. *Nature*,
770 *503*(7476), Article 7476. https://doi.org/10.1038/nature12760
771 Revelle, R., & Suess, H. E. (1957). Carbon Dioxide Exchange Between Atmosphere and Ocean
772 and the Question of an Increase of Atmospheric CO2 during the Past Decades. *Tellus*,
773 *9*(1), 18–27. https://doi.org/10.1111/j.2153-3490.1957.tb01849.x
774 Rocher-Ros, G., Sponseller, R. A., Lidberg, W., Mörth, C.-M., & Giesler, R. (2019). Landscape
775 process domains drive patterns of CO2 evasion from river networks. *Limnology and*
776 *Oceanography Letters*, *4*(4), 87–95. https://doi.org/10.1002/lol2.10108
777 Saccardi, B., & Winnick, M. (2021). Improving Predictions of Stream CO2 Concentrations and
778 Fluxes Using a Stream Network Model: A Case Study in the East River Watershed, CO,
779 USA. *Global Biogeochemical Cycles*, *35*(12), e2021GB006972.
780 https://doi.org/10.1029/2021GB006972
781 Sawakuchi, H. O., Neu, V., Ward, N. D., Barros, M. de L. C., Valerio, A. M., Gagne-Maynard,
782 W., Cunha, A. C., Less, D. F. S., Diniz, J. E. M., Brito, D. C., Krusche, A. V., & Richey,
783 J. E. (2017). Carbon Dioxide Emissions along the Lower Amazon River. *Frontiers in*
784 *Marine Science*, *4*. https://www.frontiersin.org/articles/10.3389/fmars.2017.00076
785 Stets, E. G., Butman, D., McDonald, C. P., Stackpoole, S. M., DeGrandpre, M. D., & Striegl, R.
786 G. (2017). Carbonate buffering and metabolic controls on carbon dioxide in rivers.
787 *Global Biogeochemical Cycles*, *31*(4), 663–677. https://doi.org/10.1002/2016GB005578
788 Sveinbjörnsdóttir, Á. E., Stefánsson, A., Heinemeier, J., Arnórsson, S., Eiríksdóttir, E. S., &
789 Ólafsdóttir, R. (2020). Assessing the sources of inorganic carbon in surface-, soil- and

non-thermal groundwater in Iceland by δ13C and 14C. *Geochimica et Cosmochimica Acta*, *279*, 165–188. https://doi.org/10.1016/j.gca.2020.03.021

Ulseth, A. J., Hall, R. O., Boix Canadell, M., Madinger, H. L., Niayifar, A., & Battin, T. J. (2019). Distinct air–water gas exchange regimes in low- and high-energy streams. *Nature Geoscience*, *12*(4), Article 4. https://doi.org/10.1038/s41561-019-0324-8

Venkiteswaran, J. J., Schiff, S. L., & Wallin, M. B. (2014). Large Carbon Dioxide Fluxes from Headwater Boreal and Sub-Boreal Streams. *PLOS ONE*, *9*(7), e101756. https://doi.org/10.1371/journal.pone.0101756

Wang, C., Xie, Y., Liu, S., McCallum, J. L., Li, Q., & Wu, J. (2021). Effects of diffuse groundwater discharge, internal metabolism and carbonate buffering on headwater stream CO2 evasion. *Science of The Total Environment*, *777*, 146230. https://doi.org/10.1016/j.scitotenv.2021.146230

Winnick, M. J. (2021). Stream Transport and Substrate Controls on Nitrous Oxide Yields From Hyporheic Zone Denitrification. *AGU Advances*, *2*(4), e2021AV000517. https://doi.org/10.1029/2021AV000517

Winnick, M. J., Carroll, R. W. H., Williams, K. H., Maxwell, R. M., Dong, W., & Maher, K. (2017). Snowmelt controls on concentration-discharge relationships and the balance of oxidative and acid-base weathering fluxes in an alpine catchment, East River, Colorado. *Water Resources Research*, *53*(3), 2507–2523. https://doi.org/10.1002/2016WR019724

Winnick, M. J., Lawrence, C. R., McCormick, M., Druhan, J. L., & Maher, K. (2020). Soil Respiration Response to Rainfall Modulated by Plant Phenology in a Montane Meadow, East River, Colorado, USA. *Journal of Geophysical Research: Biogeosciences*, *125*(10), e2020JG005924. https://doi.org/10.1029/2020JG005924

Winnick, M. J., & Maher, K. (2018). Relationships between CO2, thermodynamic limits on silicate weathering, and the strength of the silicate weathering feedback. *Earth and Planetary Science Letters*, *485*, 111–120. https://doi.org/10.1016/j.epsl.2018.01.005

Zhang, J., Quay, P. D., & Wilbur, D. O. (1995). Carbon isotope fractionation during gas-water exchange and dissolution of CO2. *Geochimica et Cosmochimica Acta*, *59*(1), 107–114. https://doi.org/10.1016/0016-7037(95)91550-D

Table 1. Reaction network and end-member source values for modeling experiments

Reaction Network			
Reaction	**log(K^{12}) @ 25℃**	**log(K^{13}) @ 25℃**	**log(K^{14}) @ 25℃**
$^{i}CO_{2(aq)} \leftrightarrow H^{+} + H^{i}CO_{3}^{-}$	-6.3447	-6.340835	-6.336995
$H^{i}CO_{3}^{-} \leftrightarrow H^{+} + {}^{i}CO_{3}^{2-}$	-10.3288	-10.328986	-10.32914
$H_2O \leftrightarrow H^{+} + OH^{-}$	-14*	-	-
End-member Sources			
Source	***p*CO_2 (ppm)**	**$\delta^{13}C$ (‰ VPDB)**	**$\Delta^{14}C$ (‰)**
Groundwater	20,000	-15	-500
Stream Corridor Respiration	-	-27	-66
Atmosphere	410	-9	-66

* log(K)

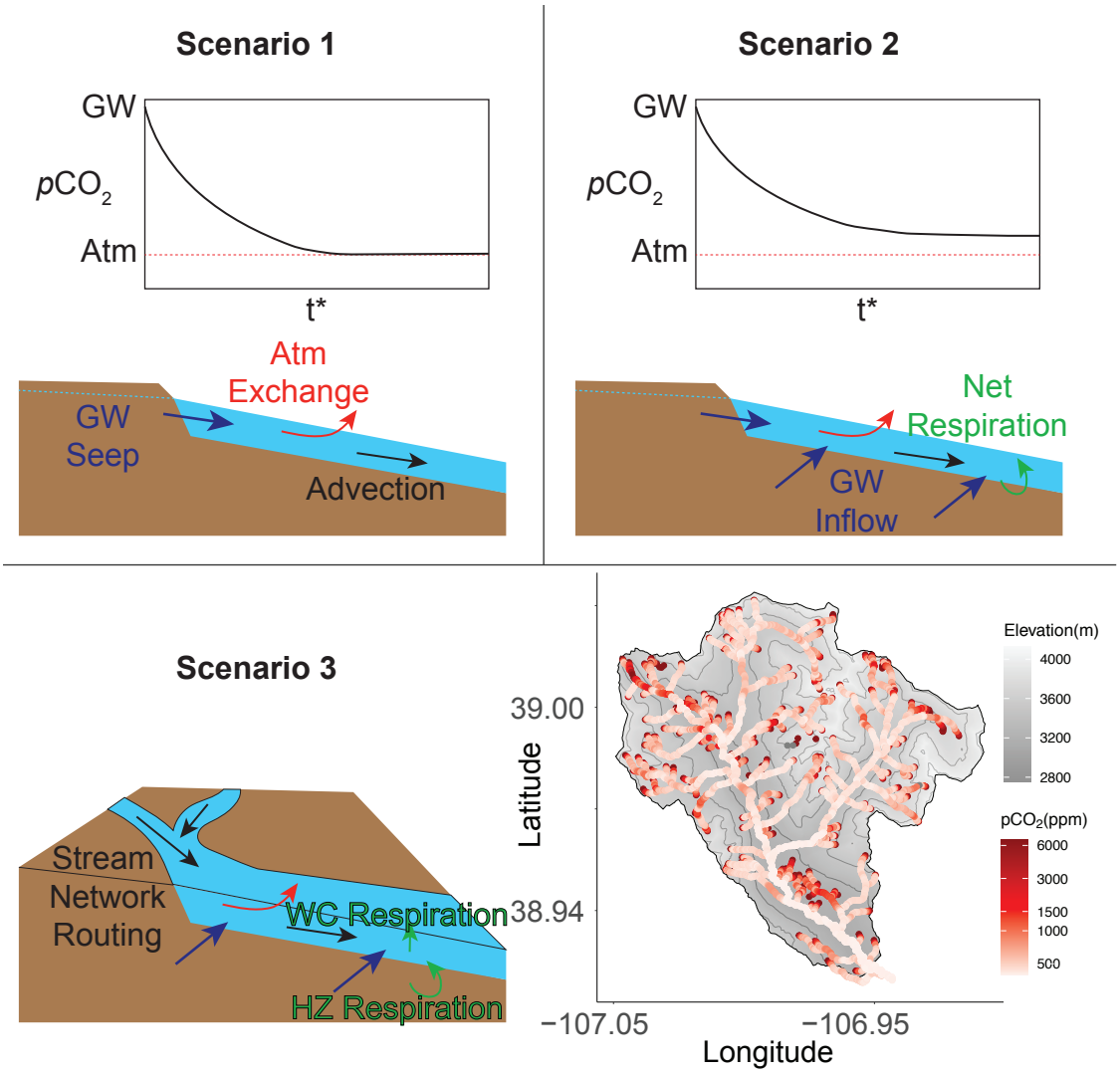

Figure 1. Conceptual diagram of the modelling scenarios including characteristic patterns of pCO_2 and the processes incorporated. Scenario 1 is analogous to a degassing GW seep with no additional CO_2 inputs. Scenario 2 represents a GW seep degassing with simultaneous CO_2 inputs from GW and stream corridor respiration, analogous to a small headwaters stream. Scenario 3 is the modeling of a full 87 km^2 5^{th} order watershed in the East River, CO, USA. It incorporates stream network water routing via advection, groundwater inputs, hyporheic exchange, net water column respiration, and atmospheric exchange. Simulated watershed pCO_2 values are from Saccardi and Winnick (2021) and represent a no-alkalinity simulation, which is compared to the updated model in Scenario 3. Note, symbol definitions translate between Scenarios, and GW Seep and Inflow end-member values are identical.

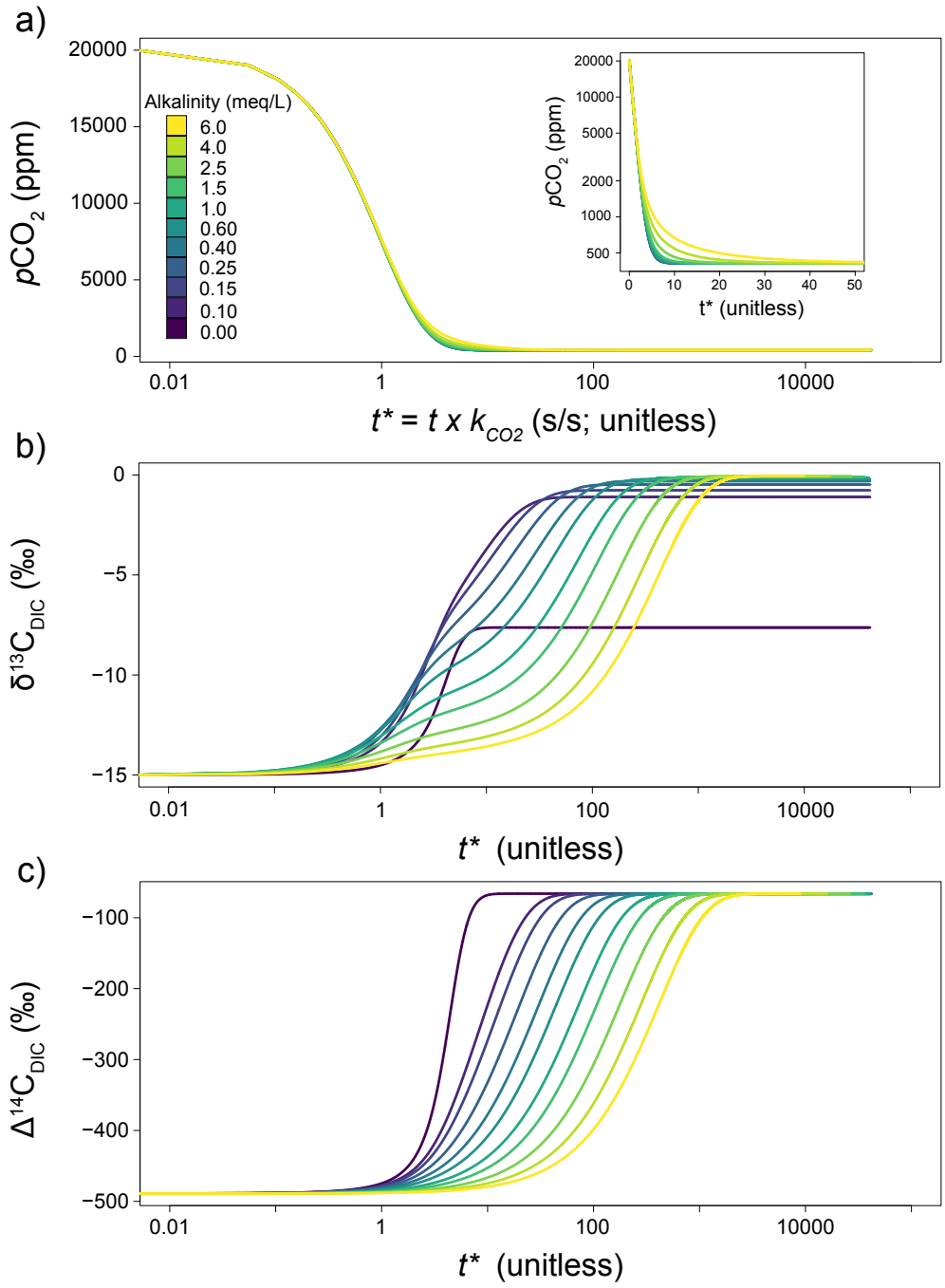

Figure 2. Temporal evolution of (a) pCO_2, (b) $\delta^{13}C_{DIC}$, and (c) $\Delta^{14}C_{DIC}$ in Scenario 1 simulations. The x-axis in all plots represents nondimensional time, calculated by multiplying simulation time (s) by the specified reaeration rate (s^{-1}). Line colors represent the specified GW alkalinity. Note the large difference between the 0 and 0.1 meq/L alkalinity lines in plot (b) reflects the non-linear decrease in the fractional contribution of $CO_{2(aq)}$ to total DIC as alkalinity increases.

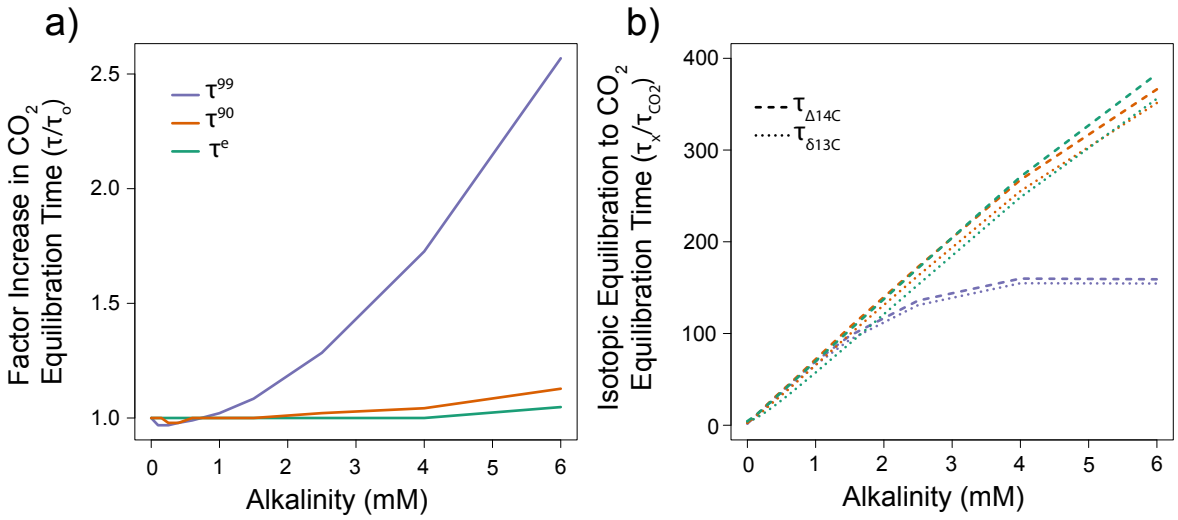

Figure 3. Impacts of alkalinity on atmosphere equilibration timescales for Scenario 1 simulations of (a) pCO_2, and (b) $\delta^{13}C_{DIC}$ and $\Delta^{14}C_{DIC}$ relative to pCO_2. Line colors represent different metrics of equilibration timescales. Dashed and dotted lines in (b) represent $\Delta^{14}C_{DIC}$ and $\delta^{13}C_{DIC}$, respectively.

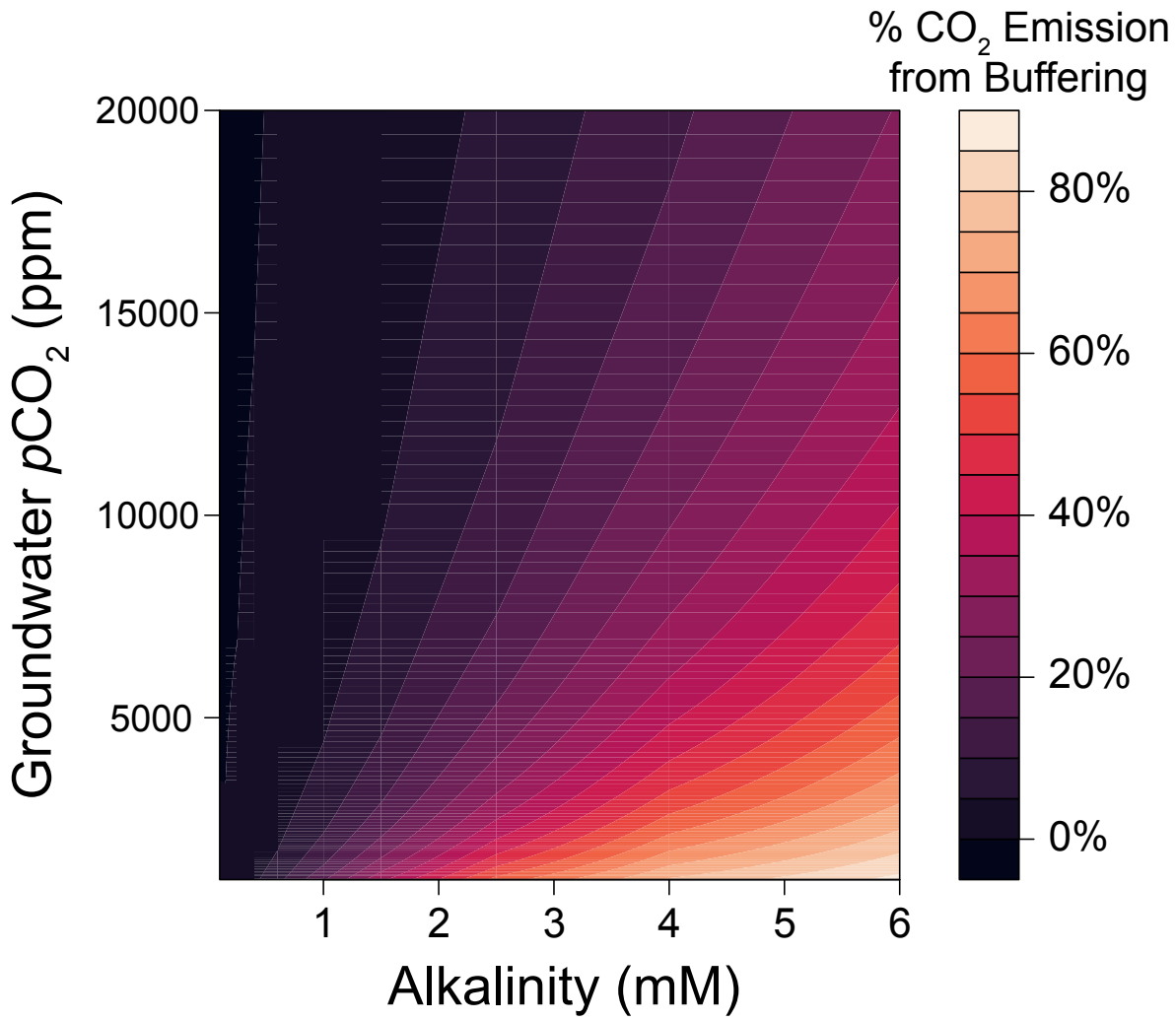

852
853
854 **Figure 4**. Contour map of the % contributions of carbonate buffering reactions to total CO_2
855 emissions in Scenario 1 as a function of GW alkalinity and pCO_2. Carbonate buffering reactions
856 contribute proportionally more to overall emissions as GW alkalinity increases and GW pCO_2
857 decreases.
858

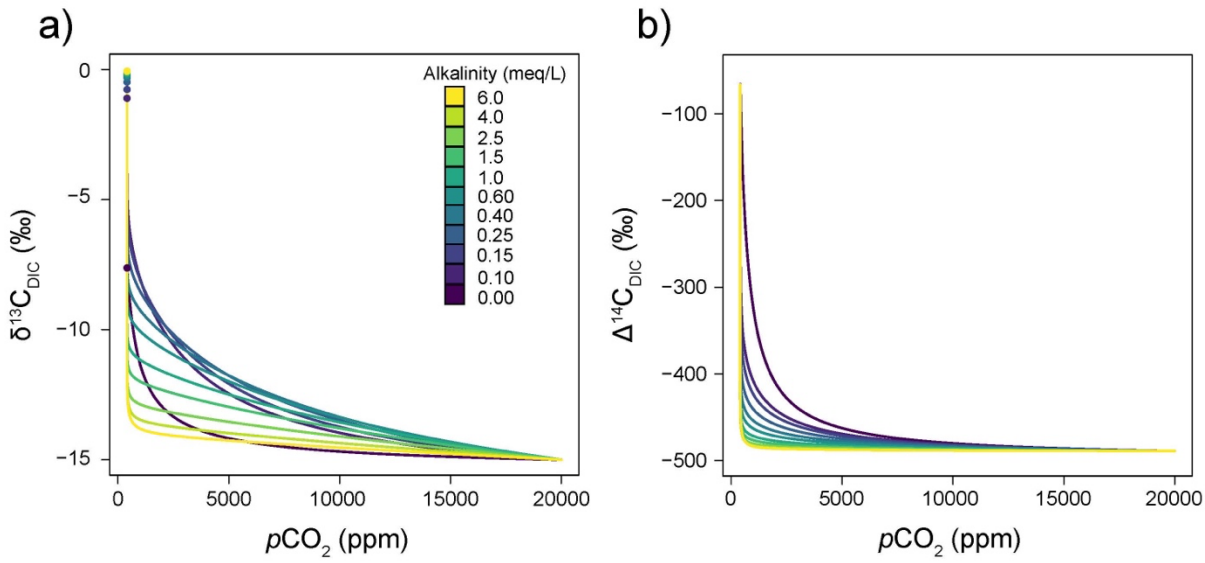

Figure 5. Covariation between pCO_2 and the isotopic composition of DIC as a function of alkalinity for (a) $\delta^{13}C_{DIC}$ and (b) $\Delta^{14}C_{DIC}$ in Scenario 1 simulations. Points in (a) represent the final atmosphere-equilibrated values, which vary with alkalinity. Notably, these patterns only represent degassing, contrasted with Figure 8 which includes degassing and input sources.

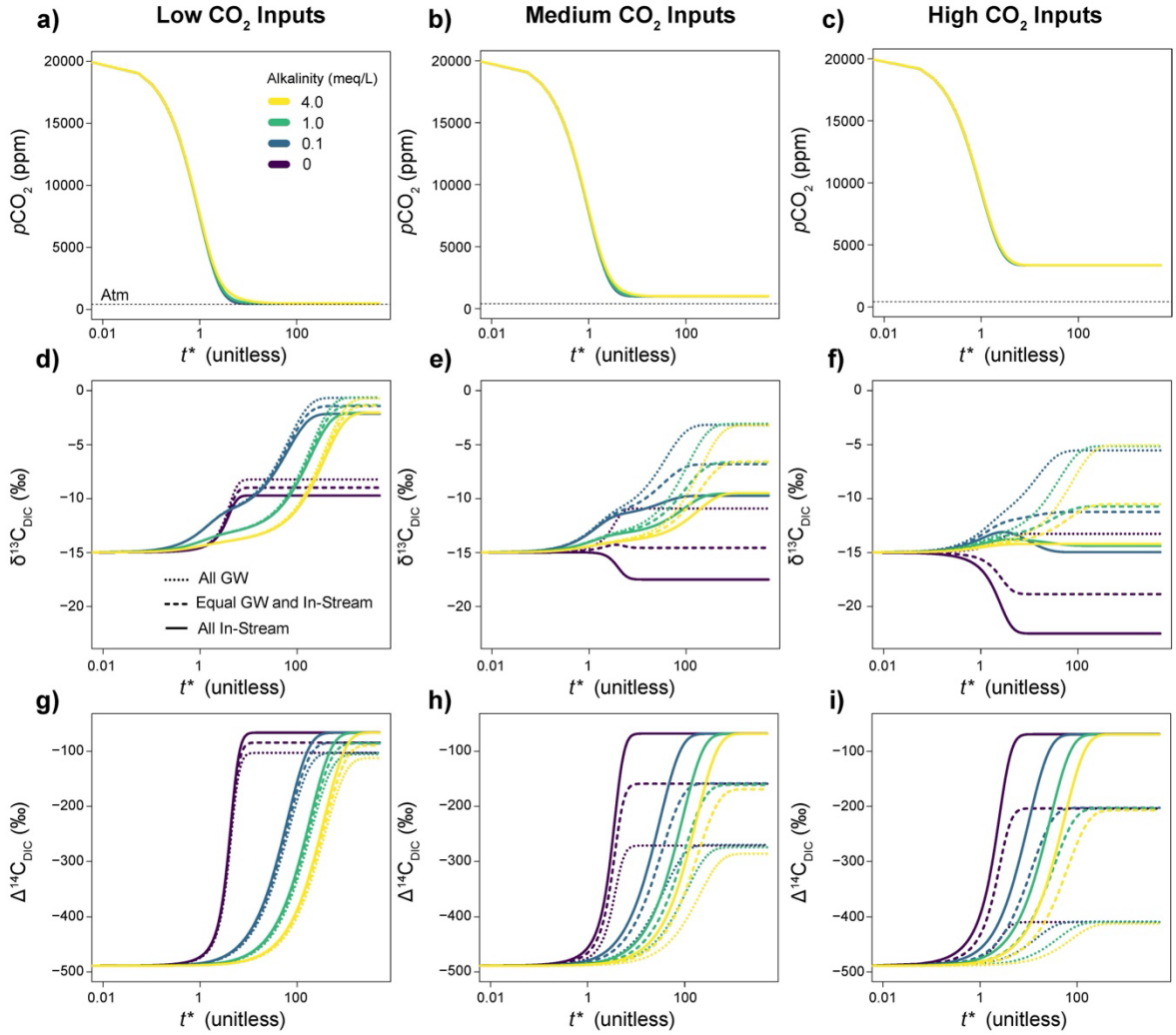

Figure 6. Temporal evolution of simulations in Scenario 2 showing pCO_2, $\delta^{13}C_{DIC}$, and $\Delta^{14}C_{DIC}$ (rows) for varying CO_2 input fluxes (columns). As in Fig. 2, x-axes represent non-dimensional time. Line color represents alkalinity, and line types represent the ratio of GW versus stream corridor respiration contributions to CO_2 inputs.

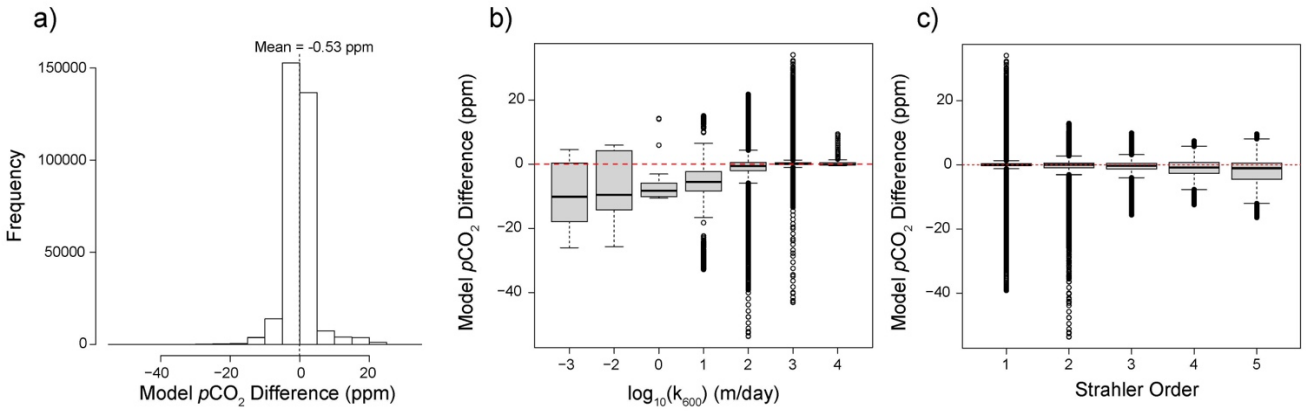

Figure 7. Comparisons of Scenario 3 simulations with 1 meq/L alkalinity and no alkalinity, showing (a) a histogram of the differences, (b) boxplot of differences binned by gas exchange velocity, and (c) boxplot of differences binned by Strahler Order. The inclusion of alkalinity results in both increased and decreased simulated pCO_2, with decreased values occurring in areas with low gas exchange rates that allow for pCO_2 to build up locally. Alkalinity does not result in increased downstream pCO_2 at the stream network scale as shown in (c).

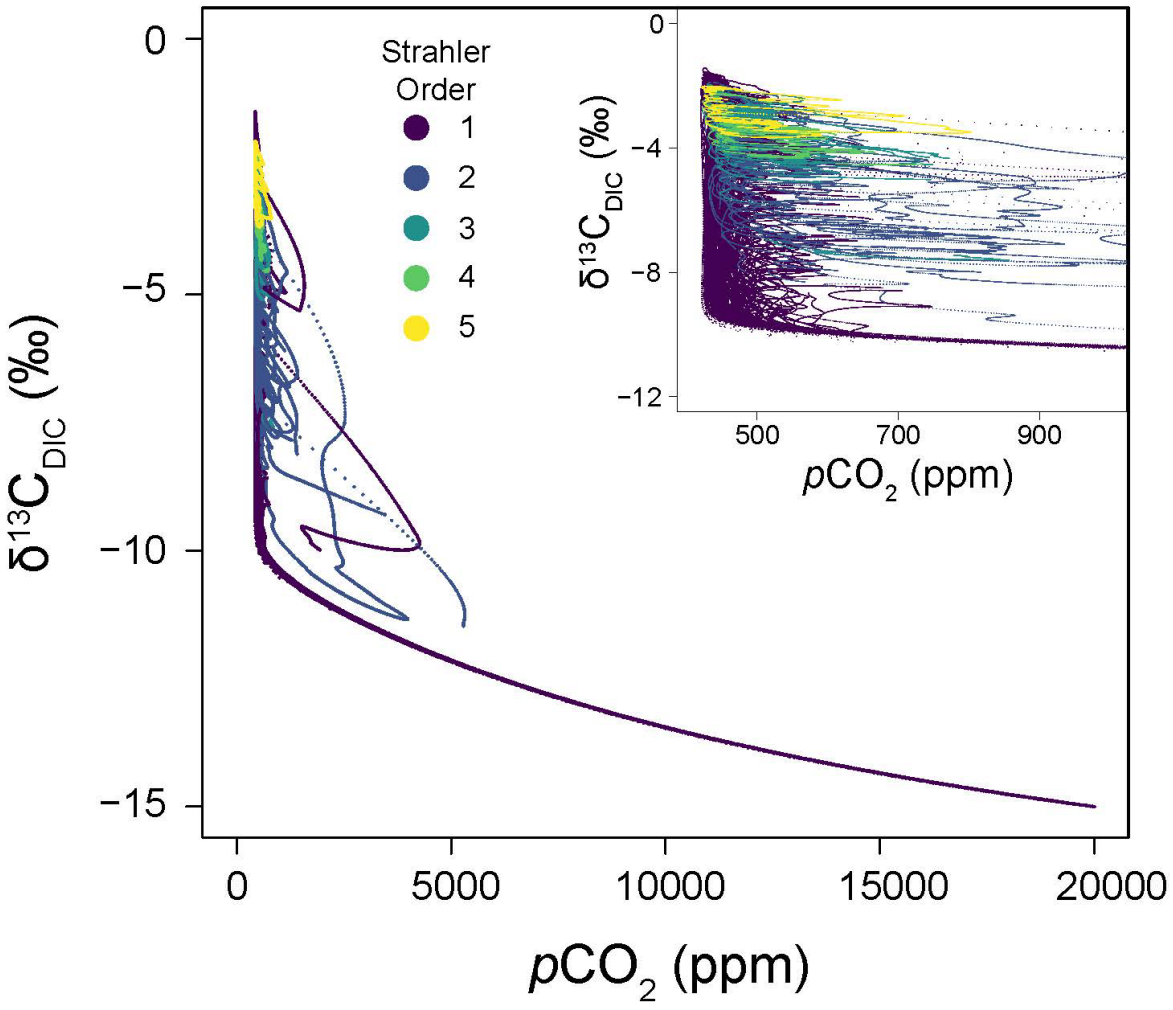

Figure 8. Simulated relationships between $\delta^{13}C_{DIC}$ and pCO_2 in the Scenario 3 simulations with 1 meq/L alkalinity. Point colors represent Strahler Order, and the inset highlights variability following GW degassing. Following GW degassing, pCO_2 and $\delta^{13}C_{DIC}$ are largely decoupled.

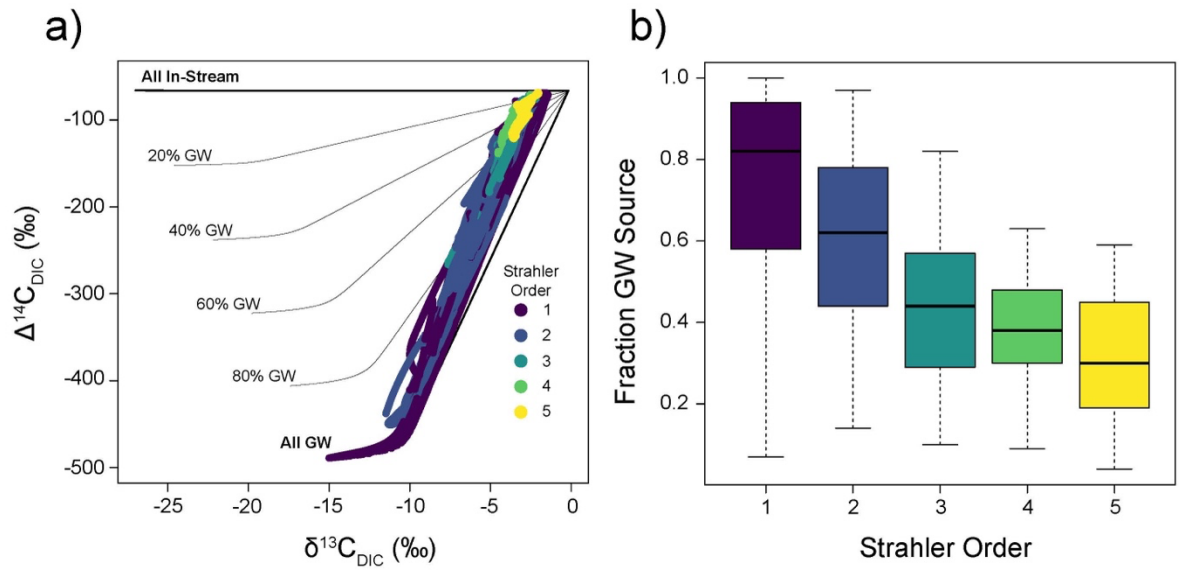

Figure 9. Carbon source partitioning using $\delta^{13}C_{DIC}$- $\Delta^{14}C_{DIC}$. (a) Simulated Scenario 3 (1 meq/L alkalinity) relationships between $\delta^{13}C_{DIC}$ and $\Delta^{14}C_{DIC}$ represent contributions from stream corridor, GW, and atmospheric end-member sources. Contour lines represent degassing simulations from mixed GW-stream corridor end-member sources. Non-linearity of the contour curves represents slight offsets in $\delta^{13}C_{DIC}$ and $\Delta^{14}C_{DIC}$ equilibration timescales (e.g. Fig. 3b). (b) Fractional contributions of DIC from GW sources (versus stream corridor respiration) as a function of Strahler Order. Simulations show a shift in sources from GW in the headwaters to stream corridor respiration in higher order streams.